Applied Materials Today 21 (2020) 100874

Contents lists available at ScienceDirect

Applied Materials Today

journal homepage: www.elsevier.com/locate/apmt

Elucidating the origin of electroplasticity in metallic materials

Moon-Jo Kim[a,1], Sangmoon Yoon[b,1], Siwook Park[b], Hye-Jin Jeong[b], Ju-Won Park[b], Kuntae Kim[b], Janghyun Jo[b], Taehoon Heo[c], Sung-Tae Hong[d], Seung Hyun Cho[e], Young-Kyun Kwon[f], In-Suk Choi[b], Miyoung Kim[b], Heung Nam Han[b,*]

[a] Shape Manufacturing R&D Department, Korea Institute of Industrial Technology, Incheon 21999, Republic of Korea
[b] Department of Material Science and Engineering & Research Institute of Advanced Materials, Seoul National University, Seoul 08826, Republic of Korea
[c] Production Engineering Group, Hyundai Steel Co Ltd, Dangjin 31719, Republic of Korea
[d] School of Mechanical Engineering, University of Ulsan, Ulsan 44610, Republic of Korea
[e] Safety Measurement Center, Korea Research Institute of Standards and Science, Daejeon 34113 Republic of Korea
[f] Department of Physics and Research Institute for Basic Sciences, Kyung Hee University, Seoul 02447, Republic of Korea

ARTICLE INFO

Article history:
Received 6 July 2020
Revised 9 September 2020
Accepted 29 October 2020

Keywords:
Electroplasticity
Plastic deformation
Defect
First principle
Finite element method

ABSTRACT

Electroplastic phenomenon has been demonstrated by that the elongation increases remarkably during deformation under electric current without a significant elevation of temperature due to Joule heating. Since the 1960s, the electroplasticity has been actively investigated; however, an exact explanation of the mechanism has been lacking. In this study, the origin of electroplasticity in metallic materials is elucidated based on first principle calculation, finite element simulation and experimental approaches. First principle calculations on a system that includes a grain boundary, which is the general defect in polycrystalline metallic materials, show that a charge imbalance near defects weakens drastically atomic bonding under electric current. The electroplastic behavior could be well reproduced with a small-scale, microstructure-based finite element simulation, which incorporates an effective temperature near defects under electric current. The effective temperature under electric current reflects the weakening of atomic bonding due to charge imbalance. In addition, the weakening of atomic bonding was confirmed by measuring the elastic modulus under electric current, which is inherently related to the atomic bonding strength. It can be said that the mechanical properties under electric current ultimately depend on the existing defects in metallic materials.

1. Introduction

There is an increasing interest in electrically-assisted manufacturing, because the application of electric current during deformation of metallic materials is expected to effectively enlarge the forming limit. Fracture strain under electric current can be significantly increased compared to the conventional uniaxial tensile test without electric current in variety of metallic materials such as aluminum alloy [1,2], magnesium alloy [3–5], titanium alloy [6–8], steel [9,10] and zinc alloy [11] (Fig. 1a–c).

Recently, various studies have reported on the athermal effects of electric current distinct from Joule heating [2,12–15]. When the athermal effect of electric current during deformation has prominence over the thermal effect, the effect is called “electroplasticity”. The electroplasticity is often demonstrated by that the elongation increases drastically during deformation under electric current without a significant elevation of temperature due to Joule heating [1,16–18]. For example, during the electric current-assisted tension of aluminum 5052-H32 alloy under pulsed electric current, the rate of increase in fracture strain was approximately 230% with reduced flow stress compared to conventional uniaxial tension (Fig. 1b). In the previous work, microstructural evidences confirm that the effect of Joule heating on the observed mechanical behavior was not dominant and that annihilation of dislocation (electrically induced annealing) occurred [2]. Schematic illustration of electroplasticity indicating how electric current influences the microstructure and mechanical behavior during plastic deformation is described in Fig. 1d. In addition to the effect on the mechanical behavior, a kinetic enhancement by electric current was observed through microstructural changes such as annealing [2,19–21], aging [1,22–24], dissolution [3,25–27], recrystallization [28–31], and microstructure healing [32,33] in metallic materials.

* Corresponding author.
E-mail address: hnhan@snu.ac.kr (H.N. Han).
[1] These authors contributed equally to this work.

https://doi.org/10.1016/j.apmt.2020.100874

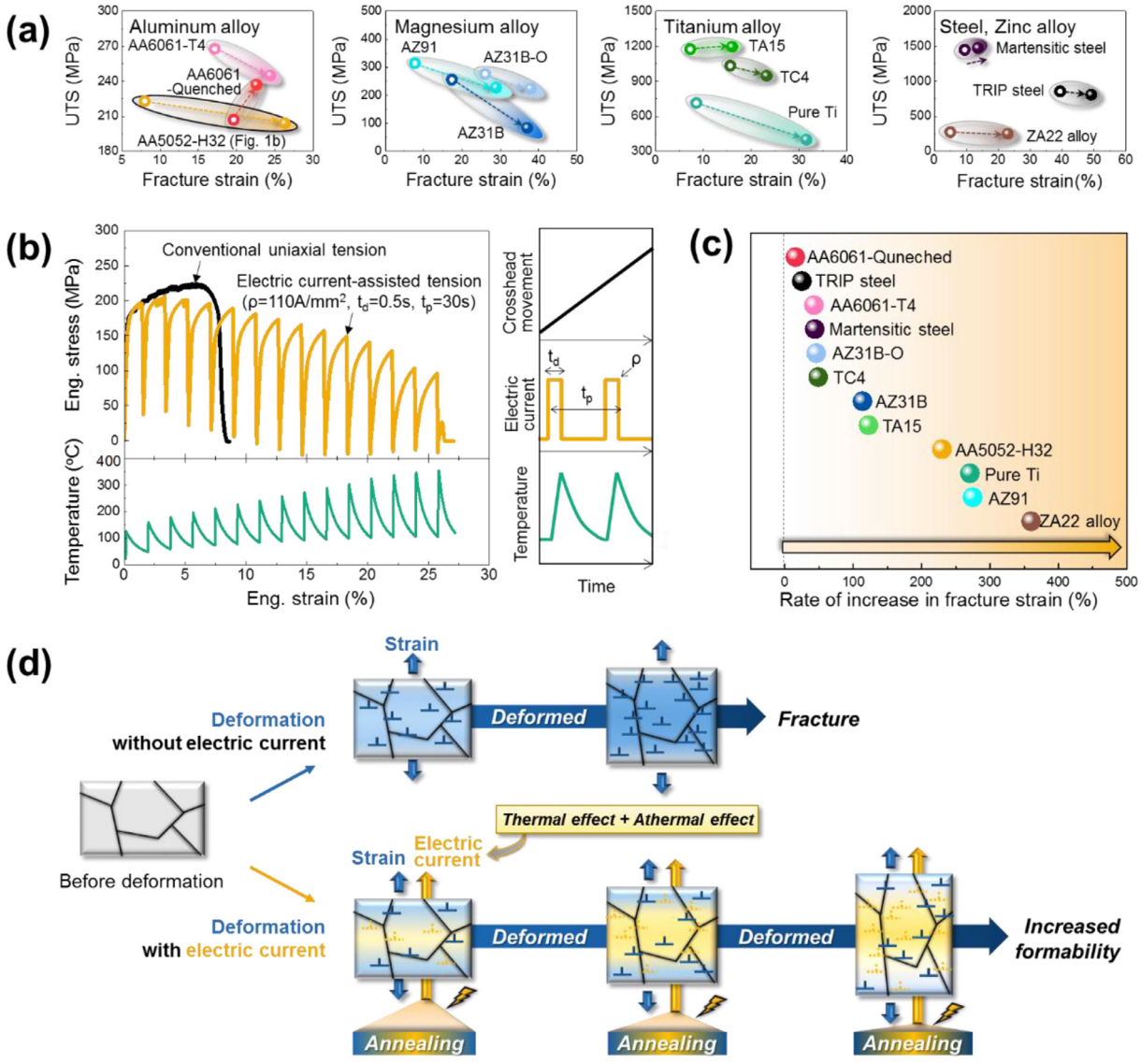

Fig. 1. Electroplastic behavior in various metallic materials. (a) Comparison of fracture strain and ultimate tensile strength (UTS) between conventional uniaxial tensile test without electric current (hollow symbol) and electric current-assisted tensile test (filled symbol, EA tension) in aluminum alloy [1,2], magnesium alloy [3–5], titanium alloy [6–8], steel [9,10] and zinc alloy [11] in literatures. (b) Engineering stress-strain curves of conventional uniaxial tensile test and electric current-assisted tensile test of aluminum 5052 alloy-H32 (AA5052-H32). A selective electrical condition (electric current density = 110 A/mm^2) was applied during plastic deformation with a set of duration (t_d = 0.5 s) and period (t_p = 30 s). (c) Rate of increase in fracture stain by applying electric current in uniaxial tensile test shown in Fig. 1a. To calculate the rate of increase in fracture strain, the difference between fracture strains in conventional uniaxial tensile test and EA tension is divided by the fracture strain in conventional uniaxial tensile test. (d) Schematic illustration of electroplasticity, indicating how electric current affects the microstructure and mechanical behavior during plastic deformation.

According to Park *et al.*, accelerated recrystallization occurred during electropulsing treatment at a temperature 100°C lower than conventional heat treatment in a furnace, even though the treatment time was similar [28]. These results strongly suggest that electric current can be utilized as an important process parameter in the design of new "electro-thermomechanical processing".

Several studies suggested that a thermal effect caused by Joule heating alone is sufficient to account for mechanical behavior changes under electric current [8,34]. They argued that an increase in temperature by Joule heating can activate the dislocation movement. However, several studies strongly reported the existence of an athermal effect of electric current. Notably, the changes in mechanical behavior or microstructure by application of electric current have been reported even under isothermal conditions [28,35,36].

Various hypotheses, which include electron wind [16,37], magnetic effect [38], and pinch effect [39], have been proposed to explain the mechanism of athermal effect of electric current. In the electron wind theory, a high density of electric current may cause interactions between moving electrons and dislocations. The range of electric current density in the electron wind theory [40] is usually $10^{4\sim6}$ A/mm^2. However, as shown in previous studies [2,3,28,41,42], the athermal effects of electric current occur even with electric current densities of $10^{1\sim2}$ A/mm^2, which is $10^{2\sim5}$ times lower than the electric current densities in electron wind theory. The electron wind force σ_{ew}acting on the dislocation movement can be calculated by the following expression: $\sigma_{ew} = C_{ew}J$, where $C_{ew}$is the electron force coefficient and $J$is the electric current density [37]. With respect to previous studies of aluminum alloys [1,41], the electron wind force acting on the dislocation movement is calculated as 10^{-4} MPa ($C_{ew} = 10^{-6}$MPa/(A/mm^2) [37] and J = 110 A/mm^2), which is significantly lower than the Peierls stress of 1~10 MPa in aluminum [43]. Therefore, the electron wind force cannot completely explain the athermal effect of electric current observed in the deformation of aluminum alloys under electric current.

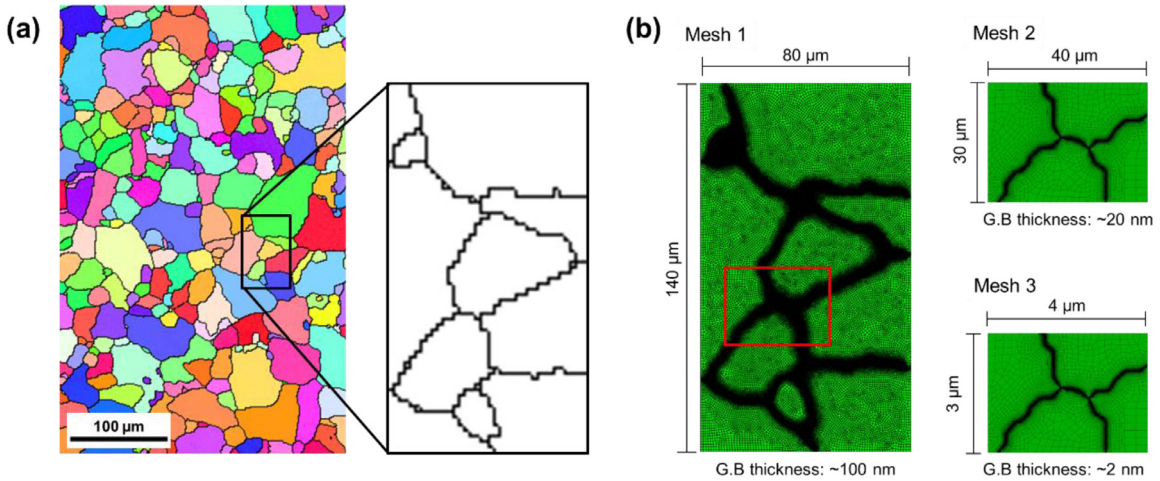

Fig. 2. Preparation of 2D mesh for FE simulation of local joule heating. (a) Inverse pole figure (IPF) map of an aluminum alloy with image quality superimposed and its corresponding grain boundary map. (b) The resulting mesh from selected areas (Mesh 1, Mesh 2, and Mesh 3, where Mesh 3 is scaled down from Mesh 2).

Magnetic effect has also been considered as the mechanism of athermal effect of electric current. The magnetic effect theory suggests that a depinning rate of dislocation is affected by the magnetic field induced by the electric current [38]. However, the magnetic effect theory can explain the electroplasticity only in limited cases where several assumptions, such as the existence of solute atoms, particle inclusions, and immobile dislocations, are essential [38,44].

Additionally, the pinch effect of compression caused by magnetic fields has been considered as a possible mechanism of electroplasticity. Pinch stress $\Delta\sigma_{\text{pinch}}$is estimated using the following equation: $\Delta\sigma_{\text{pinch}} = \upsilon_{\text{p}}\mu_{\text{m}}J^2a^2/2$, where $\upsilon_{\text{p}}$is Poisson's ratio, $\mu_{\text{m}}$is the magnetic permeability, and $a$is the sample radius [37]. The value of $\Delta\sigma_{\text{pinch}}$calculated in previous studies on aluminum alloys [1,41] is 4.379×10^{-11} MPa ($\upsilon_{\text{p}} = 0.32$, $\mu_{\text{m}} = 1.256 \times 10^{-9}$H/mm, $J = 110$ A/mm^2, and $a = 4$ mm), which would cause a negligible effect on the mechanical behavior of aluminum alloys.

As briefly discussed here, the current hypotheses may not provide clear explanation for the mechanical and microstructural behavior of metallic materials under electric current. Therefore, previously proposed mechanisms of electroplasticity remain controversial. This paper aims to clarify the underlying mechanism of electroplasticity in metallic materials with the aid of first principle calculation, finite element simulation, and experimental approaches. First, the possibility of the presence of local Joule heating and charge imbalance around grain boundaries, which are the general defects in polycrystalline metallic materials, will be investigated based on microstructure-based finite element (FE) simulation. The effect of charge imbalance on the atomic structure including a grain boundary will then be confirmed by first principle calculation and discussed related to the atomic bonding under electric current. Also, FE simulation will be conducted to describe the electroplastic behavior considering the effect of charge imbalance. Finally, the change of atomic bonding strength in electroplasticity will be investigated experimentally by measuring the elastic modulus under various electric current conditions and the underlying mechanism of electroplasticity will be discussed.

2. Modeling

2.1. Preparation of a finite element (FE) model for electrothermal behavior

To investigate the effect of electric current at grain boundaries, we conducted a FE simulation of polycrystalline structure. The microstructure of the aluminum 5052 alloy in Fig. 2a was adopted to construct a small-scale, microstructure-based model of an actual polycrystalline structure. An arbitrary region of the EBSD grain boundary map (80 μm × 140 μm) that contained a sufficient number of grain boundaries was selected. Three types of geometric meshes (Mesh 1, Mesh 2, and Mesh 3) were constructed to assume various grain boundary thicknesses as shown in Fig. 2b. To reduce the thickness of the grain boundary, Mesh 2 (40 μm × 30 μm) was selected from Mesh 1 (Fig. 2). The thicknesses of the grain boundaries in Mesh 1, Mesh 2, and Mesh 3 were assumed to be 100 nm, 20 nm, and 2 nm, respectively. It was assumed that the difference between the initial and deformed microstructures with respect to the shape of the grain is negligible for a microscale local area, such as 80 μm × 140 μm, or 40 μm × 30 μm.

The characteristics of Mesh 1, Mesh 2 and Mesh 3 are summarized in Table 1. The electrical resistivity of a grain boundary was considered to be 10 to 1000 times higher than that of the grain interior. It was assumed that the thermal conductivity of the grain boundaries increased linearly from 94.85 (W/(m•K)) to 122.85 (W/(m•K)) in the temperature range of 0-400°C and from 135.5 (W/(m•K)) to 175.5 (W/(m•K)) within the grain [45]. The electrical conductivity of the grain interior was also assumed to have a linear relationship with respect to the temperature, i.e., from 21.0438 (× 10^6, 1/Ω•m) to 10.6474 (× 10^6, 1/Ω•m) in the temperature range of 0-400°C. The material properties used for FE simulations are listed in Table 2. The electrical conductivity of grain boundaries were considered to be 1/10 (Case 1) in this work, and two additional cases with lower electrical conductivities, 1/100 (Case 2), and 1/1000 (Case 3) of those in the grain interior, are described in Supplementary Material for the case study. This variation of electrical conductivity was set to reflect the change in dislocation density in grain boundary according to plastic deformation. The applied electric current was set to 110 A/mm^2 for 0.5 s along the x and y directions.

2.2. Governing equations for thermal energy generated by electric current

Joule heating occurs when the energy dissipated by electric current is converted into thermal energy. The rate of electric energy dissipated by electric current, P, can be described as

$$P = \mathbf{J} \cdot \mathbf{E} = \frac{\partial \varphi}{\partial x} \cdot \boldsymbol{\sigma}^E \cdot \frac{\partial \varphi}{\partial x} \tag{1}$$

where $\mathbf{J}$,$\mathbf{E}$,φ, and $\boldsymbol{\sigma}^E$are the electrical current density, the electrical field intensity, the electrical potential, and the electrical conduc-

Table 1
FE mesh information for local joule heat simulation.

	Mesh 1	Mesh 2	Mesh 3
Element type		DC3D8E	
Dimension (μm^2)	80 × 140	40 × 30	4 × 3
The number of elements/nodes	772075/616772	693820/554736	693820/554736
Thickness of grain boundary (nm)	~100	~20	~2

Table 2
Material parameters of the aluminum alloy used in the FE simulation for local Joule heating. The electrical conductivity of the grain boundaries was considered to be 1/10 (Case 1), 1/100 (Case 2), and 1/1000 (Case 3) of the electrical conductivity of the grain interiors [45–47].

Parameters		Electrical conductivity ($\times 10^6$, 1/Ω·m)		Thermal conductivity (W/(m·K))		Density (kg/m^3)	Specific heat ($\times 10^3$, J/(kg·K))		Joule heat fraction
		0°C	400°C	0°C	400°C		0°C	400°C	
Grain interior		21.043	10.647	135.5	175.5	2.68	0.8718	1.0358	0.83
Grain boundary	Case 1	2.1043	1.0647	94.85	122.85	2.412			
	Case 2	0.21043	0.10647						
	Case 3	0.02104	0.010647						

tivity matrix, respectively. Typically, not all the electrical energy is converted into heat energy. Thus, by introducing an energy conversion factor (Joule heat fraction), $\eta\upsilon$, the internal heat energy released within the body can be written as $\eta\upsilon \bullet P$. In this study, $\eta\upsilon = 0.83$ was used. From the internal heat generated by electric current, one can calculate the material time rate of internal energy using the energy balance equation of

$$\int_V \rho \dot{U} dV = \int_S q dS + \int_V r dV \tag{2}$$

where V is a volume with surface area S, ρ is the density of material, $\dot{U}$is the material time rate of internal energy, q is heat flux per unit area, and r is heat supplied internally into the body. Finally, the temperature can be calculated using the specific heat of the material.

3. Results and discussion

3.1. Charge imbalances along grain boundary under electric current

In the case of electric current-assisted deformation [2,41,42], the electroplastic effect associated with reduced flow stress and/or electric current-induced annealing was more clearly observed in highly deformed states. Microstructural changes under electric current [1,3,28,48], such as recrystallization or aging behaviors, were also more significant when the materials contained many preexisting defects. These observations support the hypothesis that the electroplastic effect is associated with defects in the materials.

Grain boundaries are natural defects seen in polycrystalline solids. First, we considered the effect of local Joule heating along a grain boundary under electric current, since the electrical resistivity at a grain boundary is higher than within the grain interior [49]. Numerical simulations with two electric current directions were implemented, i.e., from left to right and from bottom to top (Fig. 3) based on previous section in Modeling. In both directions, a contour map of the temperatures for all levels of the selected grain boundary thickness shows no locally heated regions at any grain boundary. The absence of locally heated regions can be explained by rapid heat conduction in the extremely short distance between the grain boundary and the grain interior.

In order to clearly confirm that the temperature gradient does not occur between the grain interior and grain boundary under electric current, an FE analysis was additionally performed with microsecond units (10^{-6} s) and the temperature rise trend was verified. When the electric current density of $110 A/m^2$ was applied to the Mesh 2, the temperature gradient did not occur (Movie S1). This result confirms that no temperature gradient occurred due to rapid heat conduction even at the microscale level. Additional FE analysis result (Movie S1) is attached as Supplementary Material. Therefore, local Joule heating at defects does not appear to be a factor in the mechanism of electroplasticity.

Net charge is conserved by sum of the amount of incoming and outgoing charges through whole body in metal during the application of electric current. However, in local regions such as defects, which are expected to be have imperfect lattice, electron can be trapped near defects [50]. According to our FE analysis, although locally heated areas are not observed in the temperature contour maps, inhomogeneous electric current densities were observed at grain boundaries in contour map of electric current density (Fig. 3). This suggests that charge imbalances can occur at grain boundaries under electric current. If a charge imbalance exists, it is possible that the characteristics of atomic bonds near the grain boundaries could be changed.

3.2. Weakening of bonding strength under electric current

To understand the charging effects on the bonding characteristics near the grain boundaries, first principle calculation is carried out. The phonon frequency of a defect-related optical vibration mode is a direct indicator of the bonding strength of corresponding defect cores, since it is determined by the force constant matrix elements only related to the defect cores. The relation between phonon frequencies and force constants, i.e. bonding strength, can be explained even in the classical theory of lattice vibrations in the one-dimensional linear diatomic chain. Let assume two atoms with mass m and M alternately connected to each other by the force constant k. Then, the displacements of atoms are described by the two equations of motion

$$m\frac{d^2u_n}{dt^2} = -k(2u_n - u_{n+1} - u_{n-1}) \tag{3}$$

$$M\frac{d^2u_{n+1}}{dt^2} = -k(2u_{n+1} - u_{n+2} - u_n) \tag{4}$$

where u_n is the displacement of the n^{th} atom.

By solving the equations of motions, the dispersion relations of acoustic and vibrational modes in the diatomic chain are given by

$$\omega = k\left(\frac{1}{m} + \frac{1}{M}\right) \pm k\left[\left(\frac{1}{m} + \frac{1}{M}\right) - \frac{4sin^2(ka/2)}{mM}\right]^{1/2} \tag{5}$$

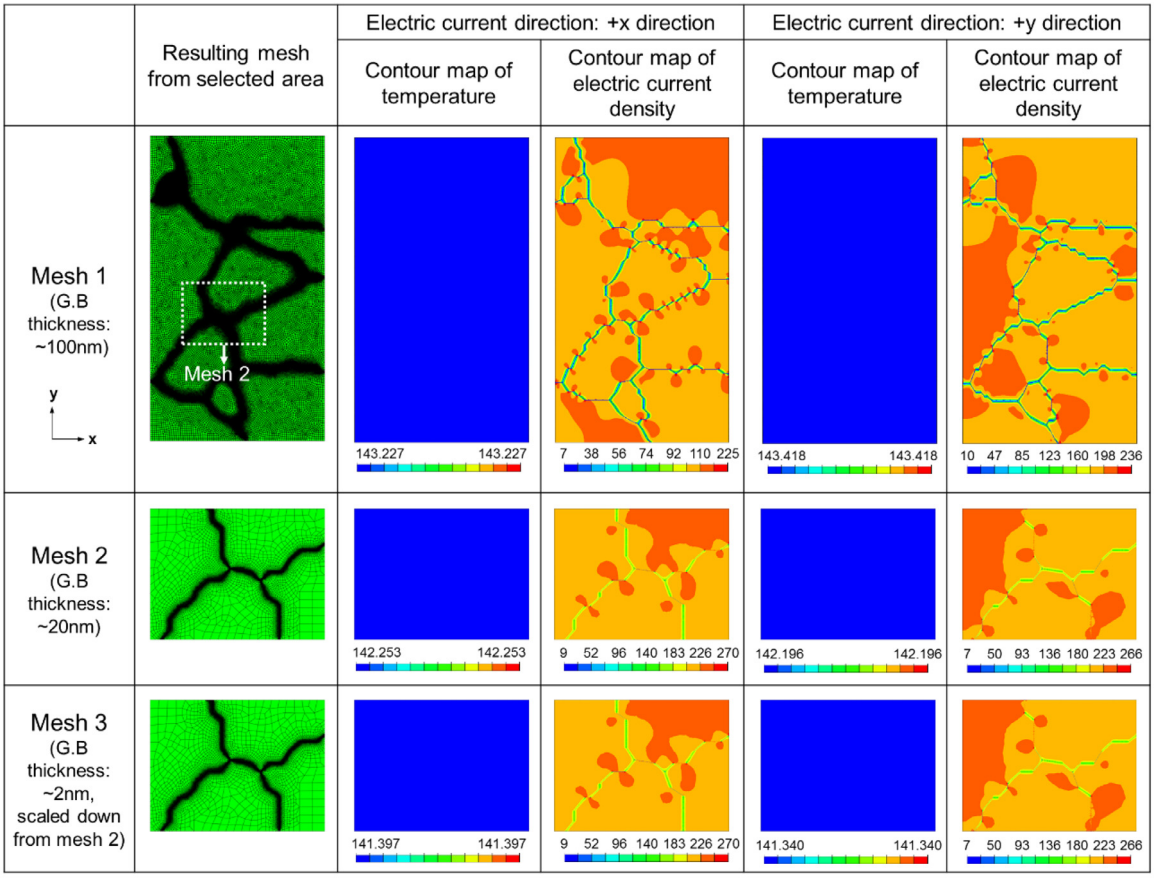

Fig. 3. Distribution of temperature and electric current density in polycrystalline under application of electric current in finite element (FE) analysis. An arbitrary region in the FE simulation is constructed based on the measured microstructure. The thickness of the grain boundary is assumed to be 100 nm to 2 nm in Mesh 1 to Mesh 3, respectively. Two directions of electric current are selected as the +x and +y directions.

Here, the frequency of optical phonon mode at the Γ point ($k = 0$) is

$$\omega_{opt} = \sqrt{2k\left(\frac{1}{m} + \frac{1}{M}\right)} \tag{6}$$

which indicates that the frequency of the optical mode is proportional to the square root of the force constant k, i.e. bonding strength. In this study, we have employed first principles calculations to extract the force constant matrix elements for the realistic atomic structure. Once the force constants are extracted, the principles to calculate the phonon dispersions are basically identical to the classical theory of lattice vibrations. Therefore, the bonding strength of defect cores can be estimated by the phonon frequencies of the optical mode localized at the corresponding cores, like the diatomic chain model.

We also claim that the phonon frequencies of defect-related optical vibrational modes are the most direct physical quantity to estimate the bonding strength of defect cores. Several other mechanical quantities, such as elastic and Young's modulus, can be estimated from first principles calculations, but it is impossible to separate the contribution of the defect cores and the bulk. It is because, in first principles calculations, the lattice defects are modeled with the periodic supercell which includes the bulk structures as well as the defect cores (see the supercell model of Σ=3 grain boundary in Experimental section). However, the phonon frequency of the localized optical vibrational mode is solely determined by the force constant matrix elements related to the defect cores. In other words, it is the physical quantity determined by the grain boundary cores even though the supercell including the bulk structures is used.

We focused on the optical vibrational mode localized at the grain boundary because it reflects the bonding characteristics of the grain boundary cores; the vibrational frequency of this mode is determined by the bonding strength. Specifically, how the localized vibrational mode is altered when one electron is added to or removed from the neutral grain boundary has been examined.

Fig. 4a shows the phonon distribution of crystalline aluminum including the $\Sigma = 3$ coincident site lattice (CSL) boundary. The $\Sigma = 3$ CSL boundary was studied as a model case (Fig. 7b), because it has the shortest periodicity among grain boundaries. The black, red, and green solid lines in Fig. 4a indicate the phonon distribution of $\Sigma = 3$ CSL boundary models in the neutral, positively-charged, and negatively-charged states, respectively. In Fig. 4a, the vibrational mode appearing from 11 to 12 THz corresponds to the optical mode localized at the $\Sigma = 3$ CSL boundary, which is confirmed by visualizing atomic vibrations in real space (Fig. 4c). Importantly, the frequency of this vibrational mode is reduced by 0.28 THz and 0.23 THz when the $\Sigma = 3$ CSL boundary is negatively and positively charged, respectively. This is the first evidence that a charge imbalance alone can weaken the bonding strength of the grain boundary cores and be a possible origin of electroplasticity.

The bonding strength of grain boundary cores from the frequency of the localized vibrational mode is estimated. Specifically, it is assumed that the optical vibrational mode is fully localized at the grain boundary region and that the atoms oscillate with harmonics. Under these assumptions, the bonding strength of grain boundary cores could be estimated as being proportional to the

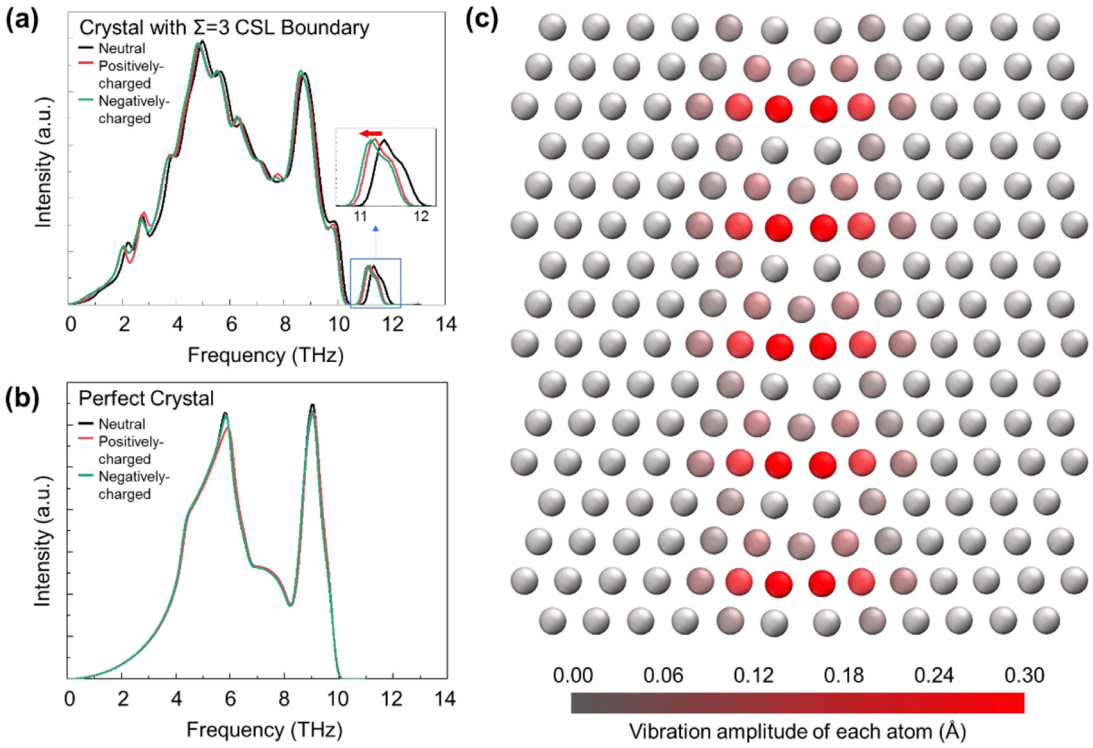

Fig. 4. Phonon distribution of (a) crystalline aluminum with the Σ = 3 coincident site lattice (CSL) boundary and (b) a perfect aluminum crystal. (c) Real space visualization of the localized vibrational mode of the Σ = 3 CSL boundary. The amplitude of each atom in this defect-related vibrational mode is represented using a color scale. The localized vibrational mode of the Σ = 3 CSL boundary appears in the range of 11 THz to 12 THz and is denoted by the arrow in Fig. 4a.

square of the frequency of the localized vibrational mode. According to the first-principles calculations, the frequencies of the optical vibrational mode localized at the Σ = 3 CSL boundary in the neutral, negatively-charged, and positively-charged states were 11.26 THz, 10.98 THz, and 11.03 THz, respectively. Therefore, the frequency reductions of the localized vibrational mode correspond to 4.87% = $(11.26^2\text{-}10.98^2)/11.26^2 \times 100\%$ and 4.01% = $(11.26^2\text{-}11.03^2)/11.26^2 \times 100\%$ reductions in the bonding strength of grain boundary cores. Here, note that the reduction in bonding strength could be substantial even though the frequency reduction of the defect-related vibration mode is relatively small.

Other vibrational modes in Fig. 4a are also lowered by about 0.1 THz, as all the vibration modes calculated in the periodic structural model (Fig. 4c) inevitably include the atomic vibrations near the Σ = 3 CSL boundary. In other words, such softening is an artifact resulting from the periodic structural model and is expected not to occur in real systems consisting of micrometer-sized grains. For comparison, Fig. 4b shows the phonon distribution of a perfect aluminum crystal without any grain boundaries. Unlike the phonon distributions of the structural model containing the Σ = 3 CSL boundary, the charge accumulation/depletion did not soften the vibrational modes of the perfect crystal at all. These results indicate that a charge imbalance only affects the bonding strength of lattices with imperfect regions, and not the perfect crystal.

3.3. Effective temperature-based electroplastic model

The density functional theory is calculated at 0 K. Therefore, the increased plasticity caused by charge imbalances near grain boundaries is obviously an athermal effect. To take into account the athermal effect in deformation behavior, the weakening of bonding strength near grain boundaries can be treated mathematically by using the concept of effective temperature at grain boundaries. Here, the effective temperature is adopted as the sum of the virtual local temperature rise and the actual temperature measured at grain boundaries to describe the mechanical responses under electric current.

An FE analysis for the electroplastic deformation, as shown in Fig. 1b, was carried out based on the isotropic linear elasticity and isotropic plasticity considering effective temperature. The temperature dependence of the elastic modulus was considered in FE simulation based on experimental data (Fig. S4). In a geometrical model of polycrystalline microstructure, the FE mesh was constructed based on the actual microstructure of an aluminum 5052 alloy as shown in Fig. 5a. The model dimensions were 72 μm × 74 μm × 1 μm with an element size of 0.5-1 μm. The numbers of elements and nodes were 6844 and 13984, respectively. The boundary conditions imposed on the FE simulation of the uniaxial tensile test under electric current are as follows (Fig. 5b): all nodes belonging to Face 2 move in the normal direction according to the experimentally set strain rate. The nodes on the Faces 2, 4, and 6 are uniformly displaced along the face normal direction whereas the nodes on Faces 1, 5, and 3 are constrained from moving along their face normal directions. The effective temperature near the grain boundary was assumed to be higher than that of the measured thermal history, and the virtual local temperature increase was set at 10°C to 55°C, which can be modulated depending on the thickness of the grain boundaries (Fig. 5a). The hardening model used in the present study assumed that the strain hardening during uniaxial tension is primarily from dislocation-dislocation interactions [51,52]. This assumption holds true when the grain size is relatively large and other hardening mechanisms are insignificant. The flow stress σ can be described as a function of dislocation density ρ_{disl} and strain rate $\dot{\varepsilon}$ as

$$\sigma = (\sigma_0 + M\beta Gb\sqrt{\rho_{disl}})\left(\frac{\dot{\varepsilon}}{\dot{\varepsilon}_0}\right)^{1/m} \quad (7)$$

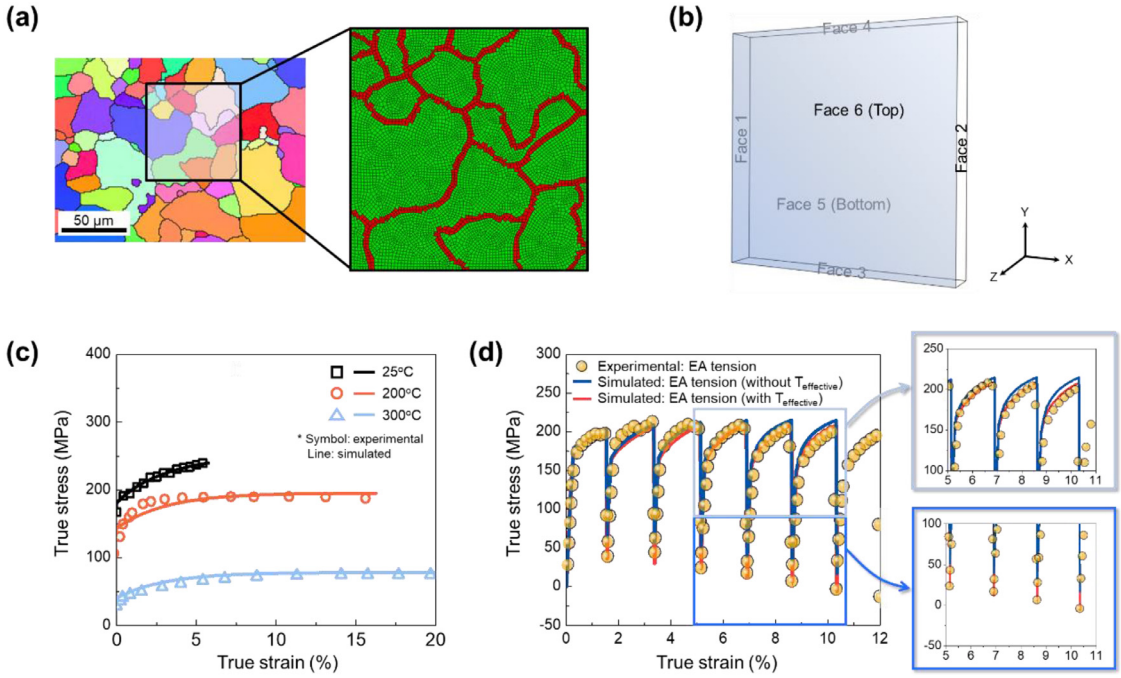

Fig. 5. (a) Inverse pole figure (IPF) map of aluminum alloy and the mesh constructed from selected area and (b) schematic image of the representative volume element for FE modeling. (c) The true stress-strain curves at different temperatures. (d) Validation of the proposed effective temperature-based electroplastic model to explain the electroplasticity observed in the aluminum alloy shown in Fig. 1b.

where *M*, *G*, and *b* are Taylor factor, shear modulus, and burgers vector, respectively, and σ_0, β, $\dot{\varepsilon}_0$, and *m*are material parameters. Here, the parameter $\sigma_0$is considered as a function of temperature and is given by

$$\sigma_0 = A \cdot T^B + C \tag{8}$$

where A, B, and C are material constants. Like σ_0, $\beta$is proposed to be

$$\beta = \lambda_1 \cdot T^{\lambda_2} + \lambda_3 \tag{9}$$

where λ_1, λ_2, and $\lambda_3$are material constants. The evolution of dislocation density is given as

$$\frac{d\rho_{disl}}{d\varepsilon} = M(K_1\sqrt{\rho_{disl}} - K_2\rho_{disl}) \tag{10}$$

The parameters $K_1$and $K_2$are used to describe the behavior of formation and recovery of dislocation, and $K_2$is known as a function of temperature and strain rate [53],

$$K_2 = K_{20} \cdot \left(\frac{\dot{\varepsilon}}{\dot{\varepsilon}_0^*}\right)^{-1/n} \tag{11}$$

where K_{20}, $\dot{\varepsilon}_0^*$, and *n*are material constants. It is suggested that the parameter *n* is a function of temperature at a low temperature region (typically $T < 0.5\ T_m$) [1]and is given by

$$n = \xi_1 \cdot \left\{T^{\xi_2}\right\} \tag{12}$$

where $\xi_1$and $\xi_2$are material parameters. The parameters introduced in this study were optimized from the stress-strain curves at different temperatures as shown in Fig. 5b.

Thermal strain was calculated from the product of thermal expansion coefficient and the temperature change by electric current. The parameters used in the hardening model and thermal properties are listed in Table 3.

Electrically-assisted (EA) tensile behaviors calculated with and without considering the effective temperature in the FE simulation are superimposed with the result of experimental EA tension in Fig. 5d. Once the electric current is applied, the stress drops sharply and the flow stress is reduced. The combined effect of thermal expansion due to increase in temperature and instantaneous annealing of the material by both thermal and athermal effects of electric current can be a the reason of the sharp stress drop behavior. Also, the instantaneous annealing during the application of electric current will influence the hardening behavior after the electric current. As shown in Fig. 5d, the experimental flow behavior cannot be fully reproduced by considering the thermal expansion and the decrease in elastic modulus caused solely by a spontaneous temperature increase. In contrast, the observed electroplastic deformation under electric current is well described by the FE simulation that incorporated the concept of effective temperature reflecting the weakening of the atomic bonding strength around the defect. It clearly shows that the athermal effect of electric current exists and the concept of effective temperature can be effectually used to describe the electroplastic behavior.

3.4. Elastic modulus under electric current

Elastic modulus is related to the resistance to separation of adjacent atoms [54–56]. In order to verify the effect of electric current on atomic bonding strength near the grain boundary, a laser ultrasonic technique was adopted to accurately measure elastic modulus under the application of electric current.

Fig. 6 shows the change in elastic modulus under the application of electric current in aluminum alloy and magnesium alloy. The measured elastic modulus under electric current is affected by both thermal effect due to Joule heating and athermal effect, so it is denoted as $E_{theraml+athermal}$ in Fig. 6. It is generally known that elastic modulus decreases with increasing temperature [57,58]. To extract the thermal effect by Joule heating on elastic modulus, $E_{thermal}$ can be estimated considering the temperature dependence on elastic modulus for each alloy (Fig. S4, Supplementary Material). For both alloys, the elastic modulus decreases with increasing electric current density. Also, the measured elastic modulus under electric current, $E_{theraml+athermal}$, in both alloys is lower than $E_{thermal}$. This indicates that the athermal effect of electric current

Table 3
Material parameters and thermal properties for FE simulation of uniaxial tensile test under electric current [45].

Hardening Model					
M	G (GPa)	b (m)	$\dot{\varepsilon}_0(s^{-1})$	m	
2.71	27	2.86×10^{-10}	3.24×10^{-6}	40.98	
K_1 (m^{-1})		K_2			
	K_{20}	$\dot{\varepsilon}_0^*(s^{-1})$	ξ_1 ($K^{-\xi_2}$)	ξ_2	
2.58×10^8	34.2	1.524×10^{-4}	0.471	0.365	
	β			σ_0	
λ_1 ($K^{-\lambda_2}$)	λ_2	λ_3	A (MPa•K^{-B})	B	C (MPa)
4.491	4.553	-0.655	-3.036×10^{-14}	5.63	102.5
Thermal Properties					
Density (kg/m^3)	Specific heat ($\times 10^3$, J/(kg•K))	Thermal expansion coefficient (μm/m• K)	Thermal conductivity (W/(m•K))		
			0 °C	400 °C	
2.68	0.88	23.8	135.5	175.5	

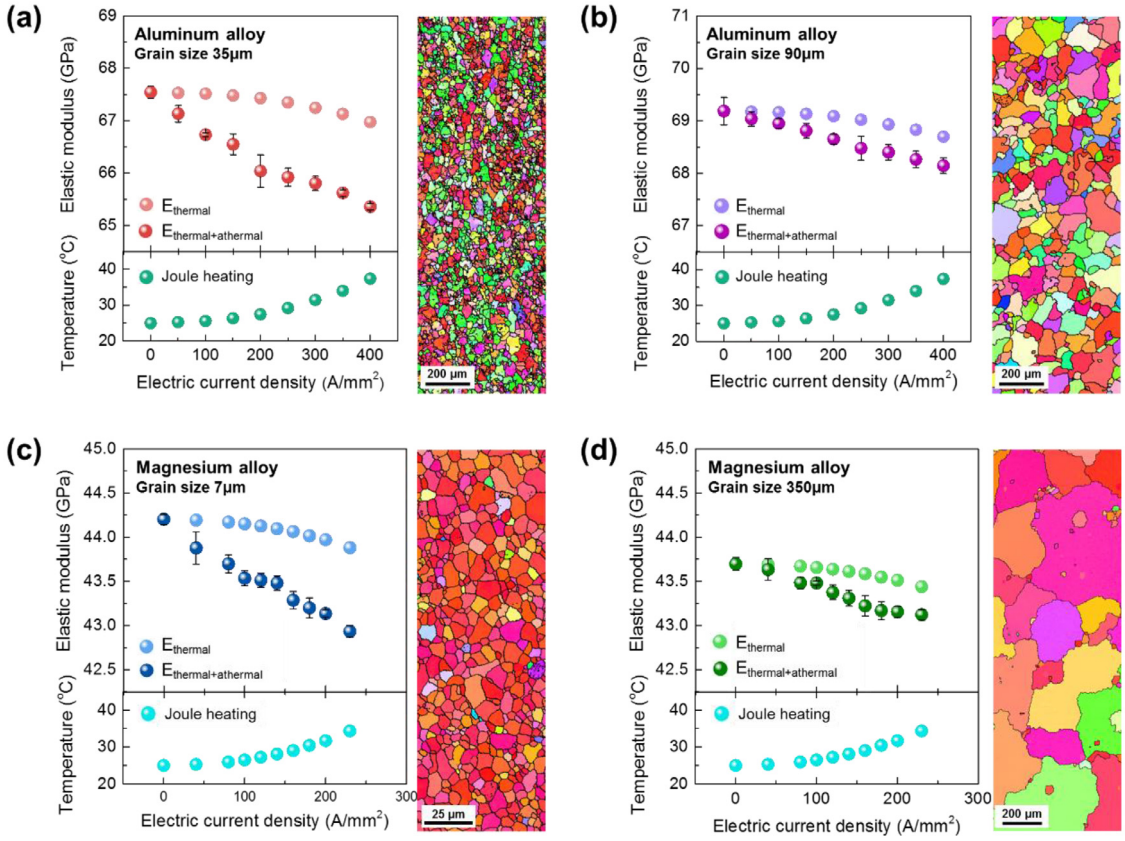

Fig. 6. Measured elastic modulus and measured temperature as a function of electric current density in aluminum alloy with grain size of (a) 35 μm and (b) 90 μm, and magnesium alloy with grain size of (c) 7 μm and (d) 350 μm. The microstructures of are shown at the right side of each graph.

can additionally weaken the atomic bonding strength in the polycrystalline.

Generally, changes in defect structure close to and in grain boundary can be significantly caused by plastic deformation. Dislocation accumulates near grain boundary, which acts as an obstacle to motion of dislocations [59,60]. Charge imbalance near grain boundary induced by electric current can soften the atomic bonding strength as confirmed in first principle calculation. The weakening of bonding strength is also confirmed by measuring elastic modulus under electric current. Basically, a fracture elongation is determined by complex relationship of various factors. It is not possible to derive a direct quantitative correlation between the increase rate of ductility and the decrease rate of elastic modulus under electric current observed in first principle calculation and experiments. However, the existence of athermal effect of electric current can additionally increase the rate of diffusion by weakening the bonding strength needed to break bond. The movement of atoms affects redistributing and eradicating the dislocation in metals, and this produces the same effect as annealing in the material by applying electric current in deformed structure. Therefore, this alteration existing dislocations can allow a metal to deform more easily, increasing its ductility with reduced flow stress during plastic deformation.

It is expected that athermal effect of electric current may occur in metallic materials, which basic material principle related to the movement of atom is involved (typically, the dislocation slip). Microstructural changes including annealing, aging, dissolution, recrystallization, and self-healing require atomic diffusion to occur. Therefore, likewise the plastic deformation under electric current, the mechanism suggested in the present research can also be used to explain the enhanced microstructural changes related to defect and diffusion.

Traditionally, heat has been a conventional process parameter to control/enhance the material behavior. The suggested underly-

ing mechanism of athermal effect of electric current is expected to provide insight of using electric current as a new process parameter in manufacturing process including forming and microstructural control of metallic materials.

In particular, it is very interesting that the effect of electric current on the decrease in elastic modulus is more significantly observed in the specimen with a smaller grain size in both aluminum and magnesium alloys. The noticeable difference between specimens with different grain sizes can be understood by the difference in grain boundary fraction. Therefore, the higher density of the charge imbalance region in both alloys with smaller grain size compared to larger grain size can explain the more significant athermal effect of electric current on the decrease in elastic modulus, i.e. decrease in atomic bonding strength under electric current. This is a clear experimental evidence of the weakening of atomic bonding by athermal effect near defects under electric current. Future investigations on the contribution of electric current related to defect density will enable accurate quantification of the athermal effect.

4. Conclusion

The origin of electroplasticity, i.e., the athermal effect of electric current, was studied based on first principle calculation, finite element simulation and experimental approaches. A microstructure-based FE simulation shows the existence of charge imbalance around grain boundaries under electric current. From first principle calculation, the charge imbalance along defects can cause weakening of atomic bonding strength. This weakening of atomic bonding strength under electric current can be mathematically described by introducing the effective temperature, which is the sum of the virtual temperature increase due to charge imbalance and the actual measured temperature. The observed electroplastic deformation under electric current could be well described by the FE simulation that incorporated the concept of effective temperature. The athermal effect on weakening of atomic bonding strength is also experimentally confirmed by measuring elastic modulus under electric current. From these results, the electroplastic phenomenon could be explained by the weakening of atomic bonding due to a charge imbalance near defects under electric current.

It can be said that the mechanical properties under electric current ultimately depend on the existing defects in metallic materials. Since electric current has proven to be an important factor in changing the microstructure or mechanical properties of a material, the application of electric current will be an important methodology in a new process called “electro-thermomechanical processing,” which might be used to develop materials with novel microstructures or mechanical properties.

5. Experimental section

5.1. Materials

Commercial aluminum 5052-H32 alloy sheets with a thickness of 2 mm were used for uniaxial tensile test and measurement of elastic modulus under electric current. For uniaxial tensile test, specimens were prepared with a thickness of 2 mm, a gauge width of 9 mm, and a gauge length of 50 mm. For measurement of elastic modulus, specimens were prepared as a long rod with a square cross section (1 mm $\times$ 1 mm $\times$ 200 mm). To make a larger grain size, the as-received specimens were heat-treated at 450°C for 7 h in a conventional box furnace, followed by furnace cooling.

Commercial AZ31B-O magnesium alloys (Mg-3Al-1Zn in wt.%.) with a thickness of 1.4 mm were also prepared to measure elastic modulus under electric current. Specimens of AZ31B-O magnesium alloys for measuring elastic modulus were prepared as a long rod with a square cross section (1.4 mm $\times$ 1.4 mm $\times$ 200 mm). Some specimens were heat-treated at 510°C for 1 h, followed by furnace cooling, to have a larger grain size.

5.2. Mechanical testing

Quasi-static uniaxial tensile test was conducted using the experimental setup described in our previous study [1] with a constant crosshead speed of 2.5 mm/min. To carry out tensile test under electric current, grip parts in the tensile machine were insulated by inserting insulation made of bakelite. A digital image correlation (DIC) system, which is a non-contact measuring technique, was used to measure displacement under electric current. Electric current was generated by DC power supply with a duration (t_d) of 0.5 s and a period (t_p) of 30 s until fracture. The electric current density was 110 A/mm^2, based on the initial cross-sectional area of the specimen. The tensile test was started when the first pulse of electric current was applied to the specimen. The temperature of specimens during tensile testing under electric current was measured using an infrared thermal imaging camera. To improve the accuracy of temperature measurement, black thermal paint was used to stabilize the emissivity, and emissivity was calibrated based on measurements with a K-type thermocouple.

5.3. Microstructural analysis

Microstructures were observed by field emission-scanning electron microscopy (FE-SEM) with an electron backscatter diffraction (EBSD) system. Specimens for microstructural analysis were prepared by a standard metallographic grinding technique. After grinding and polishing, the specimens were electropolished with an electrolyte consisting of 10% perchloric acid and 90% ethanol at approximately -20°C with a voltage of 20 V. For EBSD observation, an accelerating voltage of 15 kV and a working distance of 15 mm were used. The critical misorientation angle was set to 5° for grain identification.

5.4. First principle calculation

To study the charging effects on the bonding characteristics of grain boundaries, Vienna *Ab-initio* Simulation Package (VASP) code is used. The structural models of bulk and the $\Sigma = 3$ CSL boundary consisting of 80 aluminum atoms were used for the study (Fig. 7). Charging effects were considered by adding one electron in or removing one electron from the neutral grain boundary model. Spurious interactions between extra charges were compensated by the uniform background charge. A plane wave basis set with a cut-off of 500 eV was used to expand the electronic wave functions. Also, projector-augmented wave potentials were employed to describe the valence electrons. The exchange-correlation functional was treated with the local density approximation (LDA). The Γ-centered 3 $\times$ 1 $\times$ 4 Monkhorst-Pack k-point grid was used for reciprocal space sampling. Core structures at the $\Sigma = 3$ CSL boundary were relaxed until Hellman-Feynman forces acting on any atom were less than 0.02 eV/A. Phonon distributions were calculated using density functional perturbation theory (DFPT).

5.5. Elastic modulus measurement

To measure elastic modulus with a high accuracy, an ultrasonic method is a well-known technique, which derives elastic modulus from the ultrasonic wave velocity. This study employs a slender bar shaped specimen to apply very high density of electric current. While applying electric current, the temperature of the specimen increases instantly by Joule heating and the deformation by thermal expansion also occurs. Due to these harsh conditions,

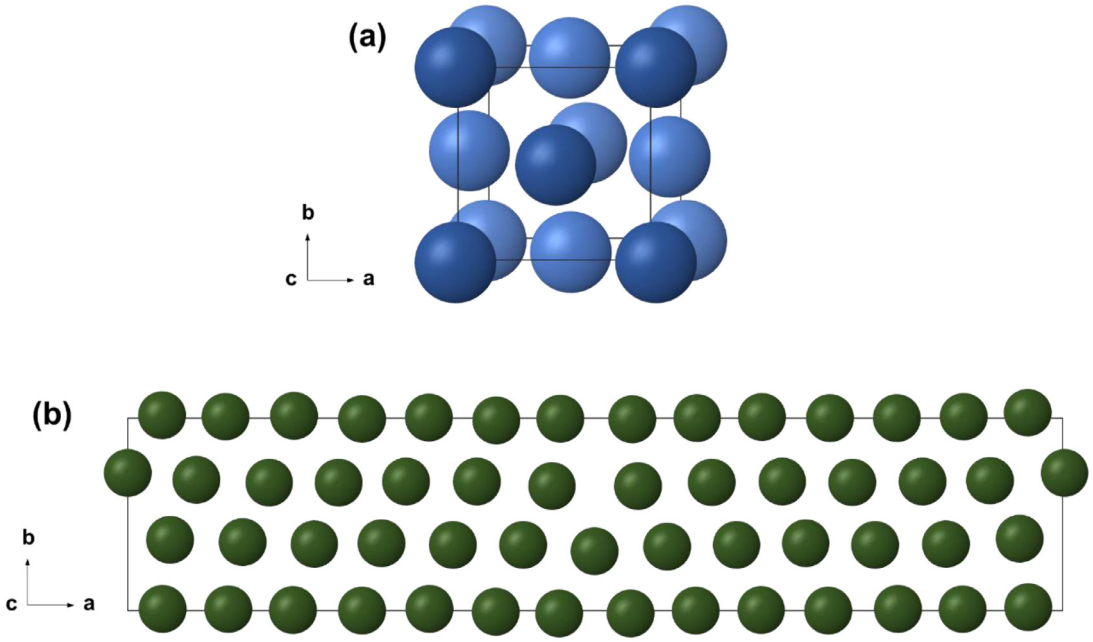

Fig. 7. Structure models used for first principle calculation: (a) bulk and (b) the Σ 3 CSL boundary. The same model structure was used for both neutral and charged states, but the core structure was individually relaxed under each condition.

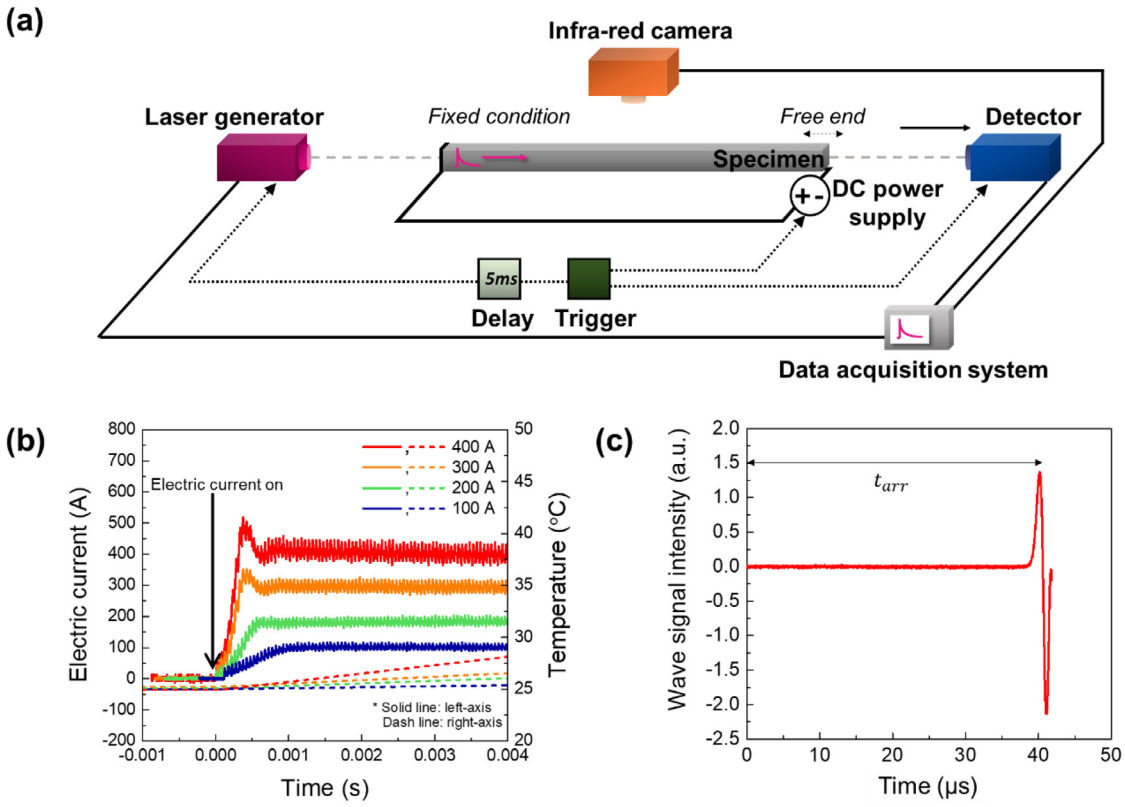

Fig. 8. (a) An illustration of the experimental setup for measuring elastic modulus under electric current. (b) Verification of stabilization time of electric current to target value after applying electric current. (c) The measured signal of the ultrasonic wave through a bar specimen.

in this study, laser based ultrasonic test was applied instead of conventional ultrasonic experiment using the piezoelectric transducers. Since the laser ultrasonic test is a non-contact method, electrical and thermal insulation can be maintained between ultrasonic transducers and a specimen. In addition, this method is applicable to a slender bar shaped specimen since the ultrasonic wave by laser can be excited and detected in point-like small spot area.

The laser ultrasonic test under very high density electric current was conducted with the experimental setup as shown in Fig. 8a. Electric current was generated by a DC power supply and flows through the bar specimen. The ultrasonic wave by a Q-switched

Nd:YAG pulse laser is excited at one end of the specimen and detected at the other end by a laser Doppler vibrometry system. Since the ultrasound propagates through a specimen less than a few tens of microseconds, the change in temperature and electric current during the ultrasound propagating are relatively negligible. Since the thermal expansion increases the length of the specimen, the specimen is fixed at one end but free at the other end in longitudinal direction to prevent its buckling, transverse deformation.

The elastic modulus is calculated from the wave velocity. In isotropic and homogenous solid media, the elastic properties such as elastic modulus, shear modulus, and Poisson's ratio can be calculated from density and the velocities of the longitudinal and shear wave, while, in case of a slender bar which its width is smaller than 1/10 of the wavelength of the propagating wave, the elastic modulus (E) from the approximated bar wave propagation model [61]can be estimated only with the longitudinal wave velocity (v_l) and the density of material (ρ) as

$$\mathrm{E} = {v_l}^2 \rho. \tag{13}$$

The approximation model is appropriate in this experiment since the width of the specimens (1 mm for aluminum alloy and 1.4 mm for magnesium alloy) are much smaller than the center wavelength (about 100 mm) excited by a pulse laser. Considering that the density of material also depends on the temperature induced by Joule heating, the elastic modulus is calculated as

$$E = {v_l}^2 \rho / (1 + \alpha (T_m - T_r))^3, \tag{14}$$

where $\alpha$is the thermal expansion coefficient. $T_m$and $T_r$are the temperature at the moment of the measurement (in Fig. 8b) and the room temperature.

Electric current was applied at the various level of electric current density based on a specimen's initial cross-sectional area. For aluminum alloys, electric current densities of 50, 100, 150, 200, 250, 300, 350, and 400 A/mm^2 were applied. For magnesium alloy, electric current densities of 40, 80, 100, 120, 140, 160, 180, 200, 230, and 255 A/mm^2 were applied to the specimen.

The temperature of specimens under electric current was measured using an infrared (IR) thermal imaging camera. The surface of each specimen was sprayed with black thermal paint to stabilize the emissivity. Fig. 8b shows the verification of stabilization time of electric current to target value after applying electric current. For the range of electric current from 100 to 400 A, it was confirmed that the electric current to target value was stabilized within 1 ms after applying the electric current. To minimize the thermal effect by Joule heating, the velocity of ultrasonic waves were measured 5 ms after applying the electric current.

The signal of the measured ultrasound at the end of the specimen is shown in Fig. 8c. The laser Doppler vibrometer detects only in out-of-plane displacement, so the measured waveform at 40 μsin Fig. 8c is a longitudinal ultrasonic wave through bar specimen in this experimental alignment. From the waveform, the arrival time (t_{arr}) is measured and the velocity of longitudinal wave can be calculated with the length of the specimen as

$$v_l = l(1 + \alpha (T_m - T_r))/t_{arr}, \tag{15}$$

where $l$is the initial length of the specimen. The reproducibility of measuring the longitudinal wave velocity in the specimen was secured for the experimental setup, and the deviation in velocity was less than 10 m/s (precision ± 0.1%). Then, the elastic modulus can be estimated by the relation as described in Eq. (14) with the calculated velocity of the longitudinal wave.

Declaration of Competing Interest

The authors declare no competing interests.

CRediT authorship contribution statement

Moon-Jo Kim: Conceptualization, Methodology, Data curation, Writing - original draft, Formal analysis. **Sangmoon Yoon:** Validation, Formal analysis, Writing - original draft. **Siwook Park:** Validation, Visualization, Formal analysis. **Hye-Jin Jeong:** Investigation, Data curation. **Ju-Won Park:** Methodology, Data curation. **Kuntae Kim:** Validation, Data curation. **Janghyun Jo:** Validation, Data curation. **Taehoon Heo:** Methodology, Data curation. **Sung-Tae Hong:** Writing - review & editing. **Seung Hyun Cho:** Methodology, Data curation. **Young-Kyun Kwon:** Formal analysis, Writing - review & editing. **In-Suk Choi:** Writing - review & editing. **Miyoung Kim:** Writing - review & editing. **Heung Nam Han:** Conceptualization, Project administration, Supervision, Funding acquisition, Writing - review & editing.

Acknowledgment

M.-J.K. is supported by the National Research Foundation of Korea (NRF) grant funded by the Korea government (MSIT) (No.2017R1C1B2012459). H.N.H. is supported by the National Research Foundation of Korea (NRF) grant funded by the Korea government (MSIT) (No. NRF-2020R1A5A6017701 and No. NRF-2018R1A2B6006856). The Institute of Engineering Research at Seoul National University also provided research facilities for this work.

Data availability

All data needed to evaluate the conclusions in the paper are present in the paper and/or the Supplementary Material. Additional data related to this paper may be requested from the authors.

Supplementary materials

Supplementary material associated with this article can be found, in the online version, at doi:10.1016/j.apmt.2020.100874.

References

[1] M.-J. Kim, M.-G. Lee, K. Hariharan, S.-T. Hong, I.-S. Choi, D. Kim, K.H. Oh, H.N. Han, Electric current-assisted deformation behavior of Al-Mg-Si alloy under uniaxial tension, Int. J. Plast 94 (2017) 148–170, doi:10.1016/j.ijplas.2016.09.010.
[2] M.-J. Kim, K. Lee, K.H. Oh, I.-S. Choi, H.-H. Yu, S.-T. Hong, H.N. Han, Electric current-induced annealing during uniaxial tension of aluminum alloy, Scr. Mater 75 (2014) 58–61, doi:10.1016/j.scriptamat.2013.11.019.
[3] H.-J. Jeong, M.-J. Kim, J.-W. Park, C.D. Yim, J.J. Kim, O.D. Kwon, P.P. Madakashira, H.N. Han, Effect of pulsed electric current on dissolution of Mg17Al12 phases in as-extruded AZ91 magnesium alloy, Mater. Sci. Eng. A 684 (2017) 668–676, doi:10.1016/j.msea.2016.12.103.
[4] M.-J. Kim, H.-J. Jeong, J.-W. Park, S.-T. Hong, H.N. Han, Modified Johnson-Cook model incorporated with electroplasticity for uniaxial tension under a pulsed electric current, Met. Mater. Int 24 (2018) 42–50, doi:10.1007/s12540-017-7297-1.
[5] H. Xie, Q. Wang, F. Peng, K. Liu, X. Dong, J. Wang, Electroplastic effect in AZ31B magnesium alloy sheet through uniaxial tensile tests, Trans. Nonferrous Met. Soc. China 25 (2015) 2686–2692, doi:10.1016/S1003-6326(15)63892-4.
[6] Z. Wang, H. Song, Effect of high-density electropulsing on microstructure and mechanical properties of cold-rolled TA15 titanium alloy sheet, J. Alloys Compd 470 (2009) 522–530, doi:10.1016/j.jallcom.2008.03.027.
[7] H. Song, Z. Wang, T. Gao, Effect of high density electropulsing treatment on formability of TC4 titanium alloy sheet, Trans. Nonferrous Met. Soc. China 17 (2007) 87–92, doi:10.1016/S1003-6326(07)60053-3.
[8] J. Magargee, F. Morestin, J. Cao, Characterization of flow stress for commercially pure titanium subjected to electrically assisted deformation, J. Eng. Mater. Technol 135 (2013) 041003, doi:10.1115/1.4024394.
[9] M.A. Lobdell, J.T. Roth, C.P. Nikhare, D. Parsons, D.-H. Yang, H.-W. Lee, S.-T. Hong, in: Proceedings of the ASME Manufacturing Science and Engineering Conference, MSEC, 2014, pp. 1–10. 2014.
[10] H.-J. Jeong, J.-W. Park, K.J. Jeong, N.M. Hwang, S.-T. Hong, H.N. Han, Effect of pulsed electric current on TRIP–aided steel, Int. J. Precis. Eng. Manuf. Technol 6 (2019) 315–327, doi:10.1007/s40684-019-00060-1.

[11] Y.H. Zhu, S. To, W.B. Lee, X.M. Liu, Y.B. Jiang, G.Y. Tang, Effects of dynamic electropulsing on microstructure and elongation of a Zn – Al alloy, Mater. Sci. Eng. A 501 (2009) 125–132, doi:10.1016/j.msea.2008.09.080.
[12] A. Rahnama, R. Qin, Room temperature texturing of austenite/ferrite steel by electropulsing, Sci. Rep. 7 (2017) 42732.
[13] K. Zheng, C. Wang, Y.-Q. Cheng, Y. Yue, X. Han, Z. Zhang, Z. Shan, S.X. Mao, M. Ye, Y. Yin, E. Ma, Electron-beam-assisted superplastic shaping of nanoscale amorphous silica, Nat. Commun. 1 (2010) 24.
[14] A.J. Sánchez Egea, H.A. González Rojas, D.J. Celentano, J.A. Travieso-Rodríguez, J. Llumà, i Fuentes, Electroplasticity-assisted bottom bending process, J. Mater. Process. Technol 214 (2014) 2261–2267.
[15] X. Liu, S. Lan, J. Ni, Experimental study of electro-plastic effect on advanced high strength steels, Mater. Sci. Eng. A 582 (2013) 211–218.
[16] H. Conrad, Electroplasticity in metals and ceramics, Mater. Sci. Eng. A 287 (2000) 276–287.
[17] J. Mai, L. Peng, Z. Lin, X. Lai, Experimental study of electrical resistivity and flow stress of stainless steel 316L in electroplastic deformation, Mater. Sci. Eng. A 528 (2011) 3539–3544.
[18] O. Guillon, C. Elsässer, O. Gutfleisch, J. Janek, S. Korte-Kerzel, D. Raabe, C.A. Volkert, Manipulation of matter by electric and magnetic fields: Toward novel synthesis and processing routes of inorganic materials, Mater. Today 21 (2018) 527–536.
[19] Z. Zhao, G. Wang, H. Hou, Y. Zhang, Y. Wang, The effect of pulsed current on the shear deformation behavior of Ti-6Al-4V alloy, Sci. Rep 8 (2018) 14748.
[20] M. Li, D. Guo, J. Li, S. Zhu, C. Xu, K. Li, Y. Zhao, B. Wei, Q. Zhang, X. Zhang, Achieving heterogeneous structure in hcp Zr via electroplastic rolling, Mater. Sci. Eng. A 722 (2018) 93–98.
[21] J. Liu, W. Liu, G. Tang, R. Zhu, Fabrication of textured Ni–9.3at.%W substrate by electropulsing intermediate annealing method, Phys. C Supercond. Its Appl 497 (2014) 119–122.
[22] Z. Wang, Y. Zhong, Z. Lei, W. Ren, Z. Ren, K. Deng, Microstructure and electrical conductivity of Cu-Cr-Zr alloy aged with dc electric current, J. Alloys Compd. 471 (2009) 172–175.
[23] Y.S. Zheng, G.Y. Tang, J. Kuang, X.P. Zheng, Effect of electropulse on solid solution treatment of 6061 aluminum alloy, J. Alloys Compd 615 (2014) 849–853.
[24] W. Wang, R. Li, C. Zou, Z. Chen, W. Wen, T. Wang, G. Yin, Effect of direct current pulses on mechanical and electrical properties of aged Cu–Cr–Zr alloys, Mater. Des 92 (2016) 135–142.
[25] X. Huang, X. Zhang, Current-driving dissolution of nanoscale brittle precipitates produced by spinodal decomposition in FeCrAl alloys, J. Alloys Compd 805 (2019) 26–32.
[26] Y. Jiang, G. Tang, C. Shek, Y. Zhu, Z. Xu, On the thermodynamics and kinetics of electropulsing induced dissolution of β-Mg17Al12 phase in an aged Mg–9Al–1Zn alloy, Acta Mater. 57 (2009) 4797–4808.
[27] C. Wu, X. Qiu, X. Xu, P. Yin, Y. Zhao, A model for rapid austenitization in steel with ferrite and pearlite microstructure under electropulsing, Materialia 6 (2019) 100343.
[28] J.-W. Park, H.-J. Jeong, S.-W. Jin, M.-J. Kim, K. Lee, J.J. Kim, S.-T. Hong, H.N. Han, Effect of electric current on recrystallization kinetics in interstitial free steel and AZ31 magnesium alloy, Mater. Charact. 133 (2017) 70–76.
[29] J. Kuang, T.S.E. Low, S.R. Niezgoda, X. Li, Y. Geng, A.A. Luo, G. Tang, Abnormal texture development in magnesium alloy Mg-3Al-1Zn during large strain electroplastic rolling: Effect of pulsed electric current, Int. J. Plast. 87 (2016) 86–99.
[30] Z. Zhao, G. Wang, Y. Zhang, Y. Wang, H. Hou, Fast recrystallization and phase transformation in ECAP deformed Ti–6Al–4V alloy induced by pulsed electric current, J. Alloys Compd. 786 (2019) 733–741.
[31] Q. Xu, G. Tang, Y. Jiang, G. Hu, Y. Zhu, Accumulation and annihilation effects of electropulsing on dynamic recrystallization in magnesium alloy, Mater. Sci. Eng. A 528 (2011) 3249–3252.
[32] Y. Zhou, J. Guo, M. Gao, G. He, Crack healing in a steel by using electropulsing technique, Mater. Lett 58 (2004) 1732–1736.
[33] H.-J. Jeong, M.-J. Kim, S.-J. Choi, J.-W. Park, H. Choi, V.T. Luu, S.-T. Hong, H.N. Han, Microstructure reset-based self-healing method using sub-second electric pulsing for metallic materials, Appl. Mater. Today 20 (2020) 100755.
[34] C. Li, S. Jiang, K. Zhang, Pulse current-assisted hot-forming of light metal alloy, Int. J. Adv. Manuf. Technol. 63 (2012) 931–938.
[35] J.S. Andrawes, T.J. Kronenberger, T.A. Perkins, J.T. Roth, R.L. Warley, Effects of DC current on the mechanical behavior of AlMg1SiCu, Mater. Manuf. Process 22 (2007) 91–101.
[36] A. Ghiotti, S. Bruschi, E. Simonetto, C. Gennari, I. Calliari, P. Bariani, Electroplastic effect on AA1050 aluminium alloy formability, CIRP Ann. Technol. 67 (2018) 289–292.
[37] A.F. Sprecher, S.L. Mannan, H. Conrad, On the mechanisms for the electroplastic effect in metals, Acta Metall 34 (1986) 1145–1162.
[38] M. Molotskii, V. Fleurov, Magnetic effects in electroplasticity of metals, Phys. Rev. B 52 (1995) 15829–15834.
[39] K. Okazaki, M. Kagawa, H. Conrad, An evaluation of the contributions of skin, pinch and heating effects to the electroplastic effect in titanium, Mater. Sci. Eng 45 (1980) 109–116.
[40] H. Ma, F. La Mattina, I. Shorubalko, R. Spolenak, M. Seita, Engineering the grain boundary network of thin films via ion-irradiation: Towards improved electromigration resistance, Acta Mater 123 (2017) 272–284.
[41] J.-H. Roh, J.-J. Seo, S.-T. Hong, M.-J. Kim, H.N. Han, J.T. Roth, The mechanical behavior of 5052-H32 aluminum alloys under a pulsed electric current, Int. J. Plast. 58 (2014) 84–99.
[42] K. Hariharan, M.-J. Kim, S.-T. Hong, D. Kim, J.-H. Song, M.-G. Lee, H.N. Han, Electroplastic behaviour in an aluminium alloy and dislocation density based modelling, Mater. Des. 124 (2017) 131–142.
[43] Y. Kamimura, K. Edagawa, S. Takeuchi, Experimental evaluation of the Peierls stresses in a variety of crystals and their relation to the crystal structure, Acta Mater 61 (2013) 294–309.
[44] V.I. Alshits, E. V. Darinskaya, M. V. Koldaeva, E.A. Petrzhik, Magnetoplastic effect: Basic properties and physical mechanisms, Crystallogra, Rep 48 (2003) 768–795.
[45] ASM International, Volume 2: Properties and Selection: Nonferrous Alloys and Special-Purpose Materials,ASM Handbook, 10th Ed., ASM International, OH, 1990.
[46] C.Y. Ho, M.W. Ackerman, K.Y. Wu, T.N. Havill, R.H. Bogaard, R.A. Matula, S.G. Oh, H.M. James, Electrical resistivity of ten selected binary alloy systems, J. Phys. Chem. Ref. Data 12 (1983) 183–322.
[47] CEN/TC 250/SC 9: ENV 199-1-2. Design of Aluminum Structures. Part 1.2. Structural Fire Design., 1997.
[48] K. Han, S. Qin, H. Li, J. Liu, Y. Wang, C. Zhang, P. Zhang, S. Zhang, H. Zhang, H. Zhou, EBSD study of the effect of electropulsing treatment on the microstructure evolution in a typical cold-deformed Ni-based superalloy, Mater. Charact. 158 (2019) 109936.
[49] H. Bross, O. Haberlen, The scattering of electrons by edge dislocations in Al, J. Phys. Condens. Matter. 5 (1993) 7687–7700.
[50] K.P. McKenna, A.L. Shluger, Electron and hole trapping in polycrystalline metal oxide materials, Proc. R. Soc. A Math. Phys. Eng. Sci. 467 (2011) 2043–2053.
[51] Y. Estrin, L.S. Tóth, A. Molinari, Y. Bréchet, A dislocation-based model for all hardening stages in large strain deformation, Acta Mater 46 (1998) 5509–5522.
[52] U.F. Kocks, H. Mecking, Physics and phenomenology of strain hardening: the FCC case, Prog. Mater. Sci. 48 (2003) 171–273.
[53] A.S. Krausz, K. Krausz, Unified Constitutive Laws of Plastic Deformation, Academic Press, Inc., California, 1996.
[54] J. Lian, S.-W. Lee, L. Valdevit, M.I. Baskes, J.R. Greer, Emergence of film-thickness- and grain-size-dependent elastic properties in nanocrystalline thin films, Scr. Mater. 68 (2013) 261–264.
[55] L. Fanton, N.B. de Lima, A. de Oliveira França Hayama, R. Caram, J.B. Fogagnolo, Texture development in cold deformed and recrystallized Ti–30Nb–4Sn alloy and its effects on hardness and young's modulus, Adv. Eng. Mater 19 (2017) 27–29.
[56] F. Wang, D. Holec, M. Odén, F. Mücklich, I.A. Abrikosov, F. Tasnádi, Systematic ab initio investigation of the elastic modulus in quaternary transition metal nitride alloys and their coherent multilayers, Acta Mater. 127 (2017) 124–132.
[57] R.B. Mclellan, T. Ishikawa, The elastic properties of aluminum at high temperatures, J. Phys. Chem. Solids 48 (1987) 603–606.
[58] H. Watanabe, T. Mukai, M. Sugioka, K. Ishikawa, Elastic and damping properties from room temperature to 673 K in an AZ31 magnesium alloy, Scr. Mater. 51 (2004) 291–295.
[59] M.L. Qi, Y. Yao, B.X. Bie, X.X. Ran, W. Ye, D. Fan, P. Li, Nucleation and growth of damage in polycrystalline aluminum under dynamic tensile loading, AIP Adv. 5 (2015) 037116.
[60] E. Pereloma, D.V. Edmonds, Fundamentals and diffusion-controlled transformations, Phase Transformations in Steels, Woodhead Publishing Ltd., 2012.
[61] K.F. Graff, Wave Motion in Elastic Solids, Dover Publications Inc., New York, 1991.